J. Fluid Mech. (2021), *vol*. 927, A12, doi:10.1017/jfm.2021.753

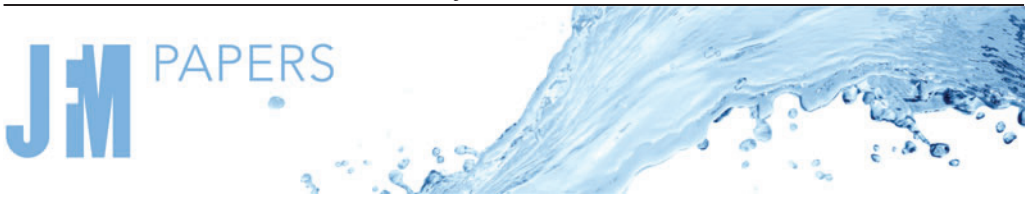

Thermohaline interleaving induced by horizontal temperature and salinity gradients from above

Junyi Li[1] **and Yantao Yang**[1,2,†]

[1]State Key Laboratory for Turbulence and Complex Systems, Department of Mechanics and Engineering Science, College of Engineering, Peking University, Beijing 100871, PR China

[2]Beijing Innovation Center for Engineering Science and Advanced Technology, Peking University, Beijing 100871, PR China

(Received 12 November 2020; revised 8 July 2021; accepted 22 August 2021)

In this work we show that horizontal gradients of temperature and salinity with compensating effects on density can drive thermohaline intrusion in the fluid layer below. Specifically, different types of double diffusive convection generate differential vertical fluxes from the top boundary, which then sustain horizontal temperature and salinity gradients within the bulk. Interleaving layers develop in the bulk and slope downward towards the cold fresh side, which are of the diffusive type. New layers emerge near the bottom boundary and shift the existing layers upward due to the density difference induced by the divergence of the vertical fluxes through the top surface. Detailed analyses reveal that the present intrusion is consistent with those in the narrow fronts, and both layer thickness and current velocity follow the corresponding scaling laws. Such intrusion process provides an extra path to transfer heat and salinity horizontally towards the cold and fresh side, but transfer the density anomaly towards the warm and salty side. These findings extend the circumstances where thermohaline intrusions may be observed.

Key words: double diffusive convection, turbulent convection, turbulence simulation

1. Introduction

Lateral gradients of temperature and salinity are omnipresent in the ocean, and thermohaline intrusions and interleaving often occur in these areas (Woods, Onken & Fischer 1986; Holbrook *et al.* 2003; Ruddick & Richards 2003; Timmermans & Marshall 2020). Thermohaline intrusions are of great importance since they generate fine-scale thermohaline structures, drive lateral flux and mixing and affect the evolution of mesoscale vortices (Merryfield 2000; Lee & Richards 2004; Ruddick, Oakey & Hebert 2010; Sarkar *et al.* 2015; Bebieva & Timmermans 2019; Tang *et al.* 2019). Numerous studies

† Email address for correspondence: yantao.yang@pku.edu.cn

have been carried out to understand the formation mechanism and transport properties of thermohaline intrusions and interleaving (Ruddick 2003; Ruddick & Kerr 2003; Krishnamurti 2006). One of the characteristic features of the interleaving is a set of vertically stacked layers with alternating current directions, and double diffusive mixing is believed to be one of the key mechanisms which induces and maintains the layering morphology (Radko 2013; Radko & Sisti 2017).

Double diffusive convection (DDC) happens when the fluid density depends on two scalars which have very different molecular diffusivities and experience certain gradients. The difference in diffusivities of temperature and salinity is usually two orders of magnitude, and the ocean is prone to double diffusive mixing (You 2002). Since the groundbreaking work of Stern (1967), various studies have proved that double diffusive mixing can generate interleaving unstable modes for different frontal configurations, which agree with the field observations in many aspects (Ruddick 2003; Ruddick & Kerr 2003; Radko 2013). The key mechanism is that the double diffusive transport between interleaving layers can further enhance the stratification and the intrusions.

In most of the existing studies, the interleaving and layering usually happen within the water mass body which experiences the vertical and horizontal gradients of temperature and salinity, such as the uniform gradient configuration and heated sidewall configuration, e.g. see Ruddick (2003), Krishnamurti (2006), Simeonov & Stern (2007) and Hebert (2011), to name a few. In those configurations, intrusion layers develop at the same depth where the scalar gradients are present. Experiments also demonstrated that the intrusion can grow near a cooled sidewall into the regions where the horizontal gradients are not preset (Malki-Epshtein, Phillips & Huppert 2004). Here, by direct numerical simulation (DNS), we reveal that surface gradients in temperature and salinity can generate horizontal gradients in the fluid layer below through double diffusive processes. These gradients subsequently lead to thermohaline interleaving and spontaneous layering. Briefly, surface gradients can be a reason for the development of intrusion underneath.

The rest of the paper is organized as follows. In § 2 we describe the flow configuration, the governing equations and the numerical method. Next, in § 3, we discuss the evolution of flow morphology from the initial field. Then, in § 4, we present analyses concerning the statistically steady state, including the interleaving layers and the horizontal transport properties. Finally, in § 5 we provide the conclusions of the study.

2. The governing equations and numerical method

We consider a Cartesian box with the height H in the z-direction and a length L in the y-direction. Gravity is in the negative z-direction. The flow is statistically homogeneous in the x-direction. At the top boundary both temperature and salinity increase along the y-direction with two homogeneous regions at the two ends. Such distributions of two scalars will simultaneously drive the convection flow in the domain. Hereafter, we respectively refer to the (x, y, z) directions as the spanwise, streamwise and vertical directions, since the convection motions are mainly in the $y-z$-plane, as shown later. An illustrative sketch of the flow configuration is shown in figure 1.

The fluid density is assumed to be linearly dependent on both temperature and salinity as $\rho^* = \rho_0^*[1 - \beta_T T^* + \beta_S S^*]$. Here, ρ^* is density with ρ_0^* being the value at the reference state; T^* and S^* are the deviations of temperature and salinity from the reference state, respectively. From now on the asterisk stands for the dimensional quantities. The parameter β_T is the thermal expansion coefficient; β_S is the coefficient of the density increase due to salinity change. The Oberbeck–Boussinesq approximation is employed for the governing

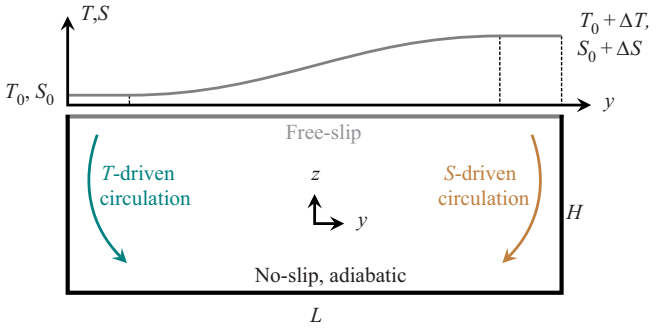

Figure 1. Sketch showing the flow domain with boundary conditions in the y–z plane. The two arrows at the two ends inside the domain indicate the direction of the convection cell if the flow is driven only by one of the two scalar gradients.

equations, which read

$$\partial_t \boldsymbol{u}^* + \boldsymbol{u}^* \cdot \boldsymbol{\nabla} \boldsymbol{u}^* = -\boldsymbol{\nabla} p^* + \nu \nabla^2 \boldsymbol{u}^* + g(\beta_T T^* - \beta_S S^*)\boldsymbol{e}_z, \tag{2.1a}$$

$$\partial_t T^* + \boldsymbol{u}^* \cdot \boldsymbol{\nabla} T^* = \kappa_T \nabla^2 T^*, \tag{2.1b}$$

$$\partial_t S^* + \boldsymbol{u}^* \cdot \boldsymbol{\nabla} S^* = \kappa_S \nabla^2 S^*, \tag{2.1c}$$

$$\boldsymbol{\nabla} \cdot \boldsymbol{u}^* = 0. \tag{2.1d}$$

Here, $\boldsymbol{u}^*$ is velocity, p^* is pressure, ν is kinematic viscosity, g is the gravitational acceleration and $\boldsymbol{e}_z$ is the unit vector in the z-direction; κ_T and κ_S are the two molecular diffusivities. In the first term on the right-hand side of (2.1a) the density has been absorbed into the pressure. We then non-dimensionalize the flow quantities by the free-fall velocity $\sqrt{g\beta_T \Delta_T H}$, the domain height H and the total scalar increments Δ_T and Δ_S along the top surface, respectively. The non-dimensional form of the governing equations is then

$$\partial_t \boldsymbol{u} + \boldsymbol{u} \cdot \boldsymbol{\nabla} \boldsymbol{u} = -\boldsymbol{\nabla} p + Pr^{1/2} Ra^{-1/2} \nabla^2 \boldsymbol{u} + (T - \Lambda S)\boldsymbol{e}_z, \tag{2.2a}$$

$$\partial_t T + \boldsymbol{u} \cdot \boldsymbol{\nabla} T = Pr^{-1/2} Ra^{-1/2} \nabla^2 T, \tag{2.2b}$$

$$\partial_t S + \boldsymbol{u} \cdot \boldsymbol{\nabla} S = Pr^{1/2} Ra^{-1/2} Sc^{-1} \nabla^2 S, \tag{2.2c}$$

$$\boldsymbol{\nabla} \cdot \boldsymbol{u} = 0. \tag{2.2d}$$

The control parameters include the Prandtl number, the Schmidt number, the thermal Rayleigh number and the density ratio, which are defined, respectively, as

$$Pr = \frac{\nu}{\kappa_T}, \quad Sc = \frac{\nu}{\kappa_S}, \quad Ra = \frac{g\beta_T H^3 \Delta_T}{\nu \kappa_T}, \quad \Lambda = \frac{\beta_S \Delta_S}{\beta_T \Delta_T}. \tag{2.3a–d}$$

Note that Ra measures the strength of the temperature difference; Λ represents the relative strength of the salinity difference compared with that of temperature difference, i.e. the ratio of the density anomaly induced by the salinity difference to that by the temperature difference. Another important parameter is the aspect ratio of the domain, namely the ratio between the domain length and height $\Gamma = L/H$.

In this study the Prandtl number is fixed at $Pr = 7$, and the Schmidt number at $Sc = 21$. Note that $Sc = 21$ is much smaller than the typical value in the ocean, of approximately $700 \sim 1000$. However, large Sc requires very fine grids and presents a big

Case number	Ra	Λ	Pr	Sc	Γ	N_x	N_y	N_z	t_{total}	$t_{statistics}$
1	10^8	1.0	7	21	4	128	512	288	28 000	20 000
2	10^9	1.0	7	21	4	128	512	288	35 000	20 000
3	10^{10}	1.0	7	21	4	192	768	384	45 000	20 000
4	10^8	1.0	7	21	8	128	1024	288	26 000	20 000

Table 1. Summary of the numerical set-up. Columns from left to right are: case number, Rayleigh number, density ratio, Prandtl number, Schmidt number, the aspect ratio of domain, the resolutions in each direction, the total simulation time and the time period during which the statistics are sampled.

challenge for DNS. Therefore, a smaller $Sc = 21$ is chosen in the present study, which is a common treatment in DDC simulations (Stellmach *et al.* 2011; Paparella & von Hardenberg 2012). Here, we set $\Lambda = 1$ so that the effects of temperature and salinity on the density compensate each other. For different cases we change Ra and Γ.

The governing equations (2.2*a*)–(2.2*d*) and the continuity equation are numerically solved by our in-house code with the finite-difference and fraction of time step method, which has been extensively used for wall-turbulence and convection flows (Ostilla-Mónico *et al.* 2015). In the present study the multi-grid method is not used, mainly due to the relatively small Schmidt number $Sc = 21$. The two endwalls in the streamwise direction are imposed by an immersed-boundary technique. The bottom wall and two endwalls in the streamwise direction are no slip for velocity and adiabatic for two scalars. The top surface is free slip and has increasing T and S along the y-direction, see the curve in figure 1. At both ends of the top surface, temperature and salinity are uniform over a width of $L/8$ with either low or high values. Between the two regions a smooth step function is used for the scalar distribution. In the spanwise direction we fix the width as H and use periodic boundary conditions. Initially, the fluid is at rest and with uniform temperature and salinity distributions at $\Delta T/2$ and $\Delta S/2$, respectively. Small perturbations are added to both scalar fields to trigger the flow.

The details of the numerical simulations are summarized in table 1. The first three cases are run with fixed aspect ratio $\Gamma = L/H = 4$, and increasing $Ra = 10^8$, 10^9 and 10^{10}. For the fourth case we use a larger aspect ratio of $\Gamma = 8$ and $Ra = 10^8$, in order to investigate the effects of the domain length. As will be shown in the following sections, the evolution of the system has a very large time scale. Therefore, the simulations have to be run for a very long time period. For example, the shortest run here is already over 25 000 non-dimensional time units. This brings up another challenge to the numerics, and only four cases are considered in the present study.

3. Development of the interleaving

We present, in this section, how the flow motions develop from the initial field and lead to the interleaving layering. Since the two endwalls and the bottom boundary are adiabatic, the total heat and salinity fluxes over the top surface should be around zero once the flow reaches the statistically steady state. Figure 2 displays the time history of these fluxes over the entire simulation of case 1, where the fluxes are measured by the Nusselt number $Nu_\zeta^{top} = (-\kappa_\zeta \partial_z \langle\zeta\rangle_{top})/(\kappa_\zeta \Delta_\zeta H^{-1})$ with $\zeta = T$ or S. Here, $\langle\cdot\rangle_{top}$ denotes the spatial average over the top boundary. For the time period $t < 3000$, the system undergoes a strong transition stage. Starting from $t \approx 3000$, oscillations emerge in the time history

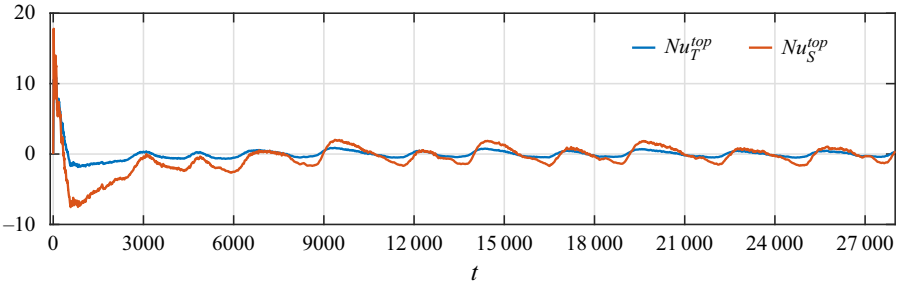

Figure 2. Time evolution of the total heat and salinity fluxes, measured by two Nusselt numbers Nu_T^{top} and Nu_S^{top}, over the top boundary for case 1.

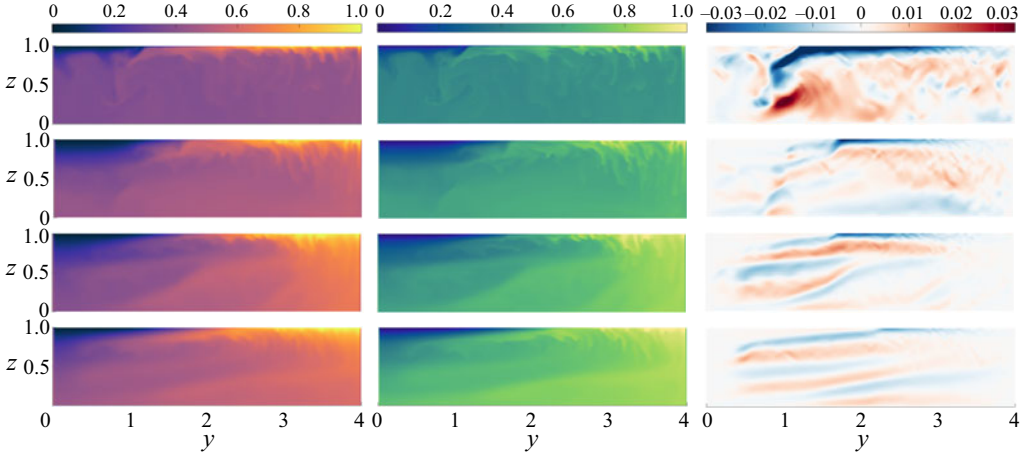

Figure 3. The development of the flow field for case 1. Rows from top to bottom are for the times 500, 1500, 3000, 9000, and columns from left to right show the fields of temperature, salinity and streamwise velocity in the spanwise mid-plane, respectively.

of the fluxes. After $t \approx 9000$, the fluxes oscillate with a stable period around 3000. This suggests that the dominant flow structures have a relatively large characteristic time scale.

The flow structures which induce the oscillations in the total fluxes are interleaving layers. In figure 3 we show the instantaneous fields of temperature, salinity and streamwise velocity on the spanwise mid-plane at four different times for case 1. Initially, both scalars have uniform distributions equal to the corresponding mean values over the top boundary. Then, just below the left half of the top boundary, the temperature and salinity differences favour the diffusive type of DDC. While on the right half, the fingering type of DDC develops. This initial stage can be seen in the top row of figure 3, where the flow structures on left and right parts have distinct horizontal scales. The different types of DDC beneath the top boundary transport heat and salinity with different rates at the two opposite sides of the domain, which sets up horizontal scalar gradients within the domain. Then interleaving layering emerges from the left side and extends horizontally towards the right side, as shown from the second to the bottom row in figure 3. Once established, these interleaving layers are the dominant structures in the flow and exhibit a complex dynamics, which will be discussed in detail in the next section.

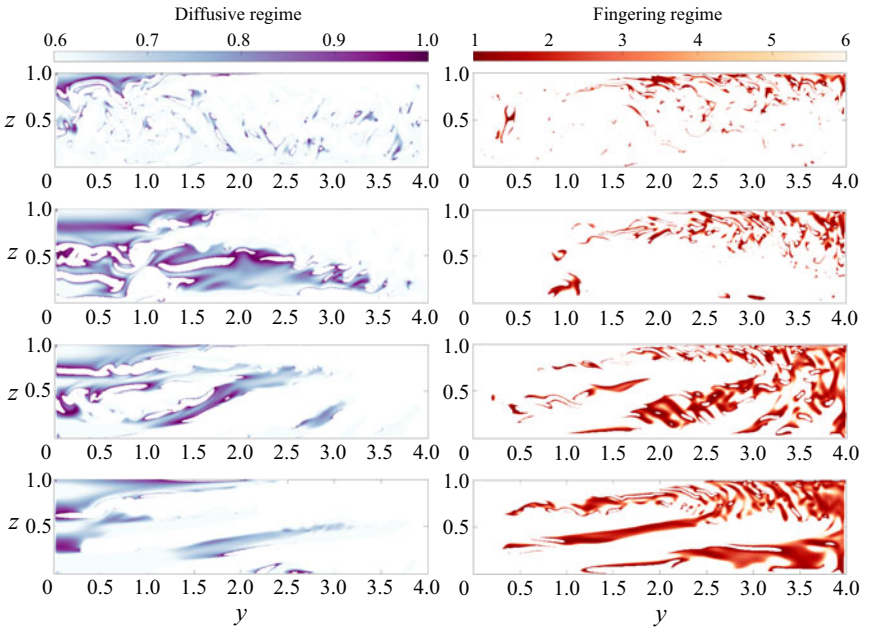

Figure 4. The evolution of the vertical density ratio Λ_z for case 1. Rows from top to bottom are for the times 500, 1500, 3000, 9000, and left and right columns show the DDC type in diffusive and fingering regimes, respectively.

The different types of DDC can be illustrated by the density ratio defined by the vertical temperature and salinity gradients. Stability theory suggests that the fluid layer is unstable to the diffusive oscillatory instability when $1 > \Lambda_z > (Pr + \tau)/(Pr + 1) = 0.917$ (Veronis 1965), and to the salt-finger instability when $1 < \Lambda_z < 1/\tau = 3$ (Stern 1960), respectively. Here, $\tau = \kappa_S/\kappa_T = 1/3$ is the diffusivity ratio between two components. In figure 4 we plot the local density ratio $\Lambda_z = (\beta_T \partial_z T)/(\beta_S \partial_z S)$ for the flow fields shown in figure 3. We highlight in the left column the region that is highly susceptible to diffusive DDC, and in the right column the region in favour of fingering DDC. Initially, both diffusive and fingering regimes are scattered throughout the domain and then the two types concentrate on the opposite sides. Note that the interleaving mainly occurs on the left part, see the bottom right panel in figure 3. The intrusion is of the diffusive type with layers sloping down to the cold and fresh side (Stern 2003). When the flow reaches the statistically stable state, both diffusive and salt-finger interfaces can be identified. These interfaces exist between the velocity interleaving layers, which we will discuss in detail in the next section.

4. Interleaving structures and horizontal transport

As shown in the previous section, once the interleaving layers are fully developed, they occupy the majority of the flow domain. The total fluxes through the top boundary exhibit long-time-period oscillations. In this section, we focus on the fully developed stage of the flow, and discuss the dynamics and transport properties of the layers. We summarize in table 2 all the key statistics from the numerical simulations, which will be discussed in detail in the following subsections.

Case number	h	$v_m(\times 10^{-2})$	$U_s(\times 10^{-4})$	Nu_T	Nu_S	Re	γ	a
1	0.194	1.45	1.50	12.0	20.6	67.7	1.768	0.234
2	0.153	1.11	1.13	19.3	33.5	142.6	1.759	0.191
3	0.145	0.94	0.69	30.4	56.9	525.7	1.706	0.106
4	0.250	1.71	0.97	17.2	30.9	158.2	1.704	0.165

Table 2. Summary of the numerical results. Columns from left to right are as follows: case number, layer thickness, the maximal current velocity, the upward-shifting velocity of the layer, Nusselt numbers for temperature and salinity, Reynolds number, the horizontal density flux ratio and the isohaline slope.

4.1. *Flow structures of interleaving*

We first show the detailed flow structures for case 2 in figures 5(*a*) and 5(*b*) by the three-dimensional volume rendering of the streamwise and vertical velocities. A stack of interleaving layers is distinctively observed in the domain. For this case seven layers are visible. The layers extend upward towards the positive streamwise direction and have alternating flow directions with a positive or negative streamwise velocity, which is a clear indication of interleaving. The layers have long horizontal length and relatively small vertical thickness. In figure 5(*c*) we plot the profiles of the temperature and salinity anomalies at seven different streamwise locations. Here, the anomaly of scalar ζ is calculated as $\zeta' = \bar{\zeta} - \overline{\bar{\zeta}}$. Hereafter, one bar stands for the spanwise average, and two bars for the spanwise and temporal average. Coherent temperature and salinity anomalies exist along the interleaving currents.

Once the flow reaches the steady quasi-periodic state, the mean temperature and salinity fields drive different types of flows within the domain. To demonstrate this, we plot in figure 6(*a*) the contours of spanwise and temporally averaged temperature and salinity fields. At the upper left and upper right corners, the isotherms and isohalines are almost horizontal and parallel. The gradients of both scalars are mainly in the vertical direction, and DDC occurs with the diffusive type near the left corner and the fingering type near the right corner. The fingering DDC generates the small-scale vertical motions on the right in figure 5(*b*). At the left part of the bulk region, where the layering is the strongest, the isotherms and isohalines have different inclination angles. By averaging over the main intrusion region, as marked by the dashed rectangular in figure 6(*a*), the mean inclination angle for isotherms is approximately 25° and that for isohalines is approximately 11°. The interleaving currents have an inclination angle of approximately 3°, which is smaller than those of the isotherms and isohalines, a phenomenon consistent with the intrusion theory (Ruddick 2003; Radko 2013).

The different types of DDC can be also identified by the Turner angle, which is defined by the vertical gradients of the mean scalars as $Tu = 135^\circ - \arg(\beta_S \partial_z \bar{S} + i\beta_T \partial_z \bar{T})$ (Ruddick 1983). Here, i is the imaginary unit, and arg stands for the argument of the imaginary number. Fingering DDC usually happens in the range $45^\circ < Tu < 90^\circ$, and diffusive DDC in the range $270^\circ < Tu < 315^\circ$. In figure 6(*b*) we present the distribution of Tu for the flow field shown in figure 5, where the mean gradients are calculated after spanwise averaging. Again, both fingering and diffusive DDC exist in the flow field. The region with $45^\circ < Tu < 90^\circ$ agrees with the vertical motions in figure 5(*b*), namely, those vertical motions are mainly fingering convection. At the upper-right corner, the fingering DDC is driven by the vertical salinity and temperature gradients imposed by the top boundary. In the left part of the bulk, the layers with fingering DDC correspond

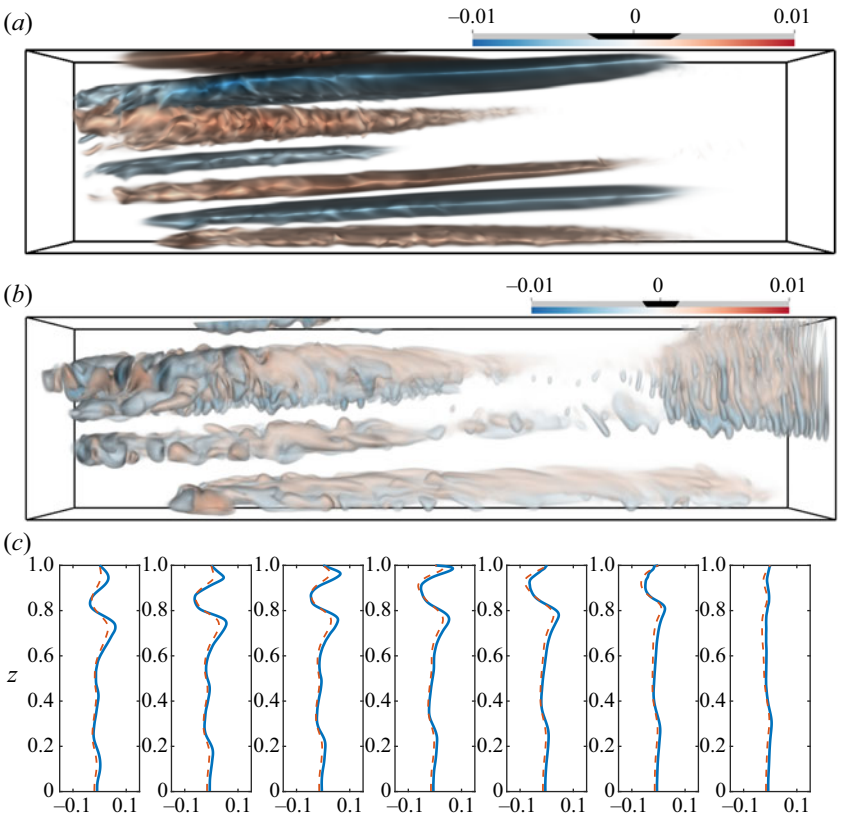

Figure 5. Thermohaline interleaving for case 2 at $t = 35\,000$ depicted by the volume renderings of (a) the streamwise velocity and (b) the vertical velocity, in which the positive y-direction is from left to right. (c) The profiles from left to right are for temperature anomaly (red dashed line) and salinity anomaly (blue solid lines) at $y = iL/8$, with $i = 1 \cdots 7$.

to the interfaces below the leftward moving currents with higher temperature and salinity and above the rightward moving ones with lower temperature and salinity. Meanwhile, diffusive DDC dominates the upper left region, where $270^\circ < Tu < 315^\circ$. The layers with $270^\circ < Tu < 315^\circ$ correspond to the interfaces above the leftward moving warm and salty currents and below the rightward moving cold and fresh ones. Different types of DDC between interleaving currents are characteristic phenomena of thermohaline intrusion (Ruddick 2003; Radko 2013).

4.2. *The upward shift of the layers*

Moreover, our numerical results reveal that the vertical location of each layer is not constant. Rather, these layers shift upward over a very large time scale, which is clearly shown in supplementary movie 1 available at https://doi.org/10.1017/jfm.2021.753. Figure 7 displays the time evolution of the vertical profiles of streamwise velocity at location $y = 3/8L$, i.e. where the interleaving currents are strongest. For case 2, it takes approximately 10 000 non-dimensional time units for one layer to move from the bottom to the top surface. Detailed investigation indicates that the total density difference between the two ends in the streamwise direction periodically changes sign, and close to the bottom boundary new layers are generated accordingly with alternating movement directions.

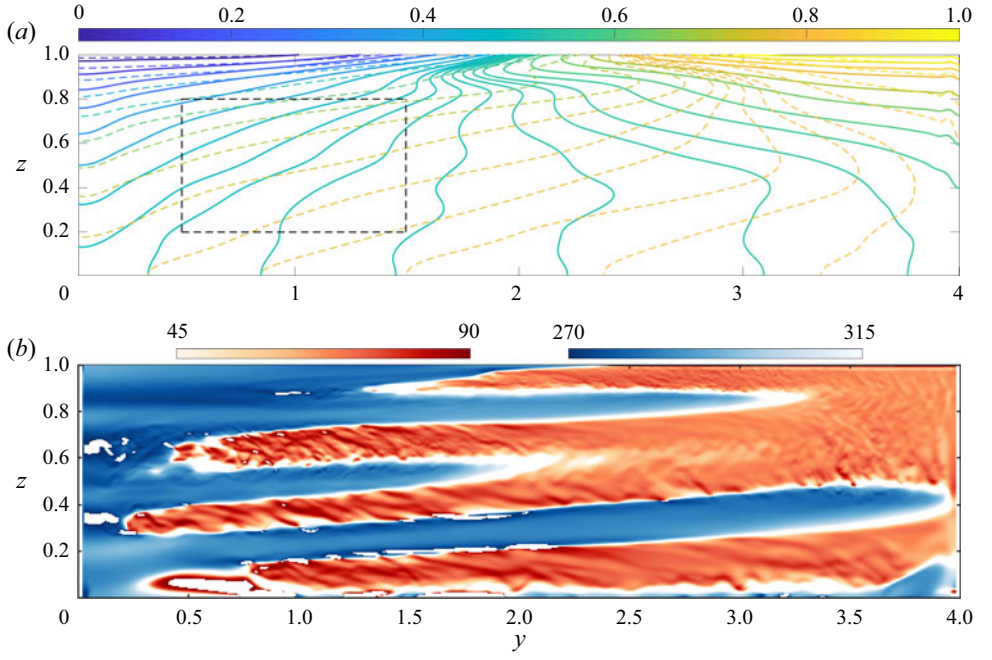

Figure 6. (*a*) Contours of spanwise and temporally averaged temperature $\overline{\bar{T}}$ (solid lines) and salinity $\overline{\bar{S}}$ (dashed lines). (*b*) Flow regions susceptible to different types of double diffusion. Colours represent the Turner angle Tu, with blue colours indicating the diffusive type and red colours the fingering type, respectively. Here, Tu is calculated by the spanwise averaged scalar gradients $\partial_z \bar{T}$ and $\partial_z \bar{S}$ for the flow field shown in figure 5.

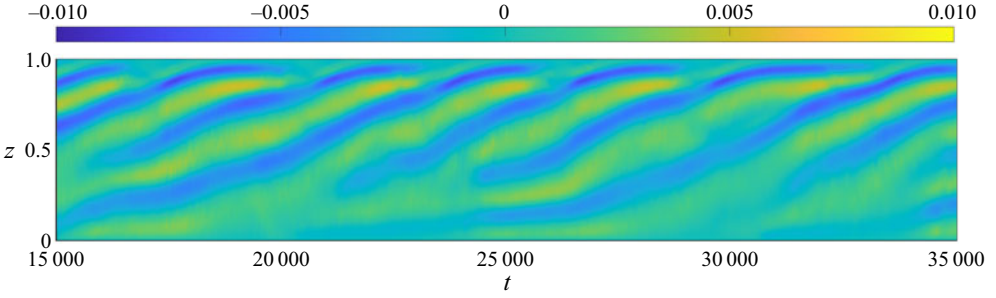

Figure 7. The upward shifting of the interleaving layers depicted by the time evolution of the spanwise-averaged profiles of the streamwise velocity at the streamwise location $y = 3L/8$ for case 2.

From the contours in figure 7 we extract the upward-shifting velocity U_s of the layers. Specifically, within the height range $0.2 < z/H < 0.8$, we calculate the auto-correlation coefficient of $\bar{v}$ for the height separation δz and the time separation δt. Then, the shift velocity U_s is determined by the location of the maximal auto-correlation coefficient on the δz–δt plane. The values are given in table 2. Compared with the current velocity, the shift velocity U_s is much smaller, by approximately two orders of magnitude.

The upward shift is caused by the continuously emerging new layers near the bottom boundary, which are generated by the periodically oscillating density difference between the two ends of the domain. This lateral asymmetry may be the key reason for the upward migration. It should be mentioned that the linear instability analysis revealed a

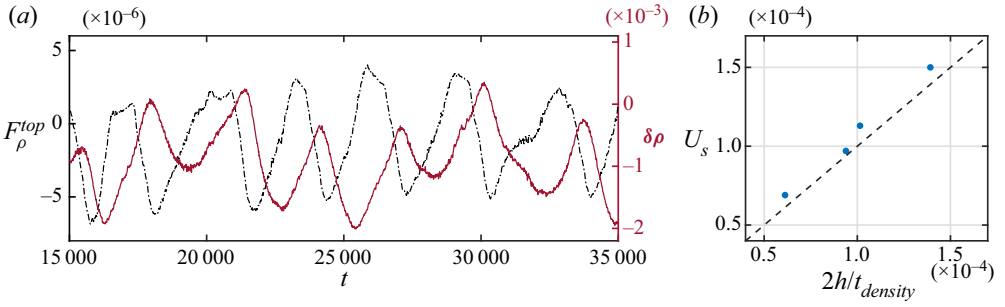

Figure 8. (*a*) The time histories of density flux through the top surface Nu_ρ^{top} (black dash-dotted line and left ordinate) and the mean density difference $\delta\rho$ (red solid line and right ordinate) between $y = 7L/8$ and $L/8$ for case 2. (*b*) The upward-shifting velocity U_s vs $2h/t_{density}$ with h being the layer thickness and $t_{density}$ the period of the $\delta\rho$.

migration of the unstable modes in the heated sidewall configuration (Kerr 1989). We calculate the difference of mean density over two streamwise locations $y_1 = 7L/8$ and $y_2 = L/8$, namely $\delta\rho = \langle\rho'\rangle_{y_1} - \langle\rho'\rangle_{y_2}$. Here, $\langle\,\rangle_y$ stands for the spatial average over the streamwise cross-section at the location y. The density is calculated as $\rho' = \Lambda S - T$. The total density flux through the top surface is measured accordingly as $F_\rho^{top} = \kappa_T\langle\partial_z T\rangle_{top} - \kappa_S\Lambda\langle\partial_z S\rangle_{top}$. In figure 8(*a*) we plot the time histories of $\delta\rho$ and F_ρ^{top} for case 2. Both quantities fluctuate with a similar period. Moreover, the variation of $\delta\rho$ lags behind F_ρ^{top} by a phase difference of approximately $\pi/2$. From the time history of $\delta\rho$ we can extract the mean period of oscillation $t_{density}$. If we assume that for each period two layers develop near the bottom boundary, then the upward-shifting velocity U_s should be very close to the velocity scale $2h/t_{density}$. This is indeed the case, as shown in figure 8, where all data points are very close to the line $U_s = 2h/t_{density}$.

4.3. *Statistics of interleaving layers*

One of the key parameters of intrusion is the layer thickness h. Previous experiments by Ruddick & Turner (1979) (RT experiments) found the scaling law of h_{RT}, which is proportional to the so-called Chen scale (Chen 1974) developed for the bounded intrusion model. Later, Toole & Georgi (1981) obtained another scale h_{TG} for the unbounded case. These two scales were then proven to be the two end limits in asymptotic analysis for the intrusion front width, which was demonstrated by Niino (1986) and Simeonov & Stern (2004) in different ways. The latter also introduced an extra scale h_{SS} for an intermediate state. Here, we will first use Niino's (1986) method to reveal that the fronts are narrow enough in our cases (the same as in the RT experiments) and then demonstrate that the layer thickness in our simulations indeed has a scaling law which is essentially the same as that for h_{RT}. It should be pointed out that the model developed in Simeonov & Stern (2004) requires a preset vertical density ratio Λ_z and its relation with Nusselt number $Nu(\Lambda_z)$ for the fingering regime. In our configuration, however, both fingering and diffusive regimes are present simultaneously, so it is difficult to estimate Λ_z or $Nu(\Lambda_z)$. Actually, the Niino (1986) theory also applies to the fingering regime, but he demonstrated that the theory is valid for the diffusive cases as far as the salt fingers are present, which is satisfied in our simulations.

Case number	Δ_S^h	G	ϵ	μ	R	$40(1+\mu)^{5.4}$	$2\times10^5(1+\mu)^{4.9}$
1	0.391	0.582	1.020	−0.116	0.570	20.6	1.09×10^5
2	0.260	0.144	0.628	−0.127	0.230	19.2	1.03×10^5
3	0.157	0.061	0.369	−0.162	0.164	15.4	0.84×10^5
4	0.539	0.751	0.680	−0.098	1.105	23.0	1.21×10^5

Table 3. Summary of the key parameters in the Niino (1986) model. Columns from left to right are as follows: case number, the lateral variation of salinity across the front, the frontal stability parameter, the modified Schmidt number, the stratification parameter, the modified stability parameter and the low and high critical values for determination of the front width. When $R < 40(1+\mu)^{5.4}$, the front can be considered narrow and the layer thickness has a scaling law the same as h_{RT} (Ruddick & Turner 1979). When $R > 2\times10^5(1+\mu)^{4.9}$, the front can be considered wide and the layer thickness has a scaling law the same as h_{TG} (Toole & Georgi 1981).

The following parameters are required in the Niino (1986) theory: the frontal stability parameter $G = (g(1-\gamma_f)\beta_S\Delta_S^h/2)^6/(K_S^2 l^2 N^{10})$, the modified Schmidt number $\epsilon = \nu/K_S$, the stratification parameter $\mu = g(1-\gamma_f)\beta_S\partial_z\overline{\overline{S}}/N^2$ and the modified stability parameter $R = G/\epsilon$. Here, γ_f is the flux ratio for fingering DDC and we use the constant value 0.88 since the diffusive ratio τ equals 1/3, which was also used in RT experiments. Also, K_S is the eddy diffusivity of salinity and we calculated it in the same way as Nu_S (see § 4.4); l is the half-width of the intrusion front and we assume it to be of the same order as $L/2$ since the interleaving layers nearly occupy the whole bulk area in all cases; Δ_S^h is the lateral variation of salinity within the water mass; and $N = \sqrt{-(g/\rho)\partial_z\rho}$ is the buoyancy frequency. In the RT experiments, both the lateral salinity variation and the vertical scalar stratification are carefully set as the control parameters, which is not the case in our simulations. Instead, we take Δ_S^h as the averaged salinity difference between two endwalls in the streamwise direction, and calculate N and $\partial_z\overline{\overline{S}}$ by the mean density and salinity difference between the top and bottom boundaries. The results are summarized in table 3. The fronts can be considered narrow when $R < 40(1+\mu)^{5.4}$, and obviously our results fall into this range. Thus, h should have the same scaling law for h_{RT}. Note that $\mu < 0$ indicates the diffusive regime in our cases. As mentioned above, Niino (1986) demonstrated that the theory is still valid for $-1 < \mu < 0$ as long as salt fingers are present. The values of G and R are much smaller than those in the RT experiments (Niino 1986). This may be attributed to the small Δ_S^h, which is qualitatively consistent with the Simeonov & Stern (2004) theory.

Now we would like to examine the scaling law of layer thickness, which is sampled from individual spanwise mean profiles at $y = 3L/8$ and averaged over time and all layers. Since in the present flows the fronts are narrow and the layer thickness should follow the RT scaling $h_{RT} = C_h(g\beta_S\Delta_S^h)/N^2$ (Ruddick & Turner 1979; Niino 1986), in figure 9(*a*) we plot h vs $(g\beta_S\Delta_S^h)/N^2$. Indeed the data follow the scaling law with $C_h \approx 0.066$.

Another parameter that has been widely studied is the maximum horizontal velocity v_m of the interleaving layers. For the different frontal widths and DDC types, previous experiments (Ruddick & Turner 1979) and simulations (Simeonov & Stern 2007, 2008) all observed the same scaling law $v_m \sim C_v Nh$ with different values for the prefactor C_v. We use the spanwise-averaged profiles at $y = 3L/8$ to find the maximal horizontal velocity v_m of all layers during the whole sampling period. The result is consistent with the previous

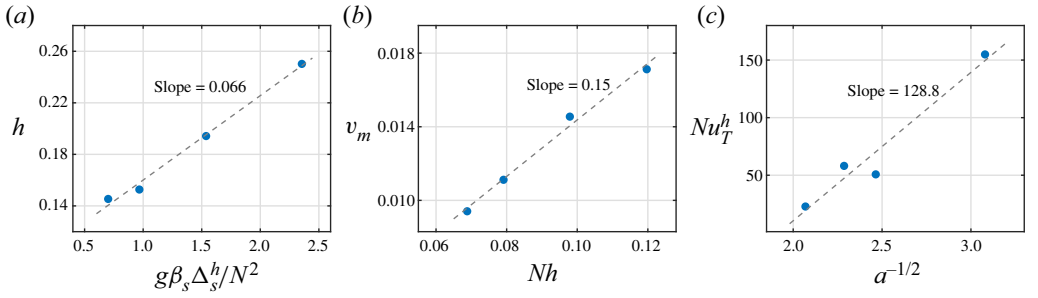

Figure 9. Properties of the interleaving layers. (*a*) Layer thickness h vs $(g\beta_S\Delta_S^h)/N^2$. (*b*) The maximal current velocity v_m vs Nh. (*c*) The horizontal heat flux Nu_T^h vs $a^{-1/2}$ with a being the isohaline slope.

work and the prefactor C_v is approximately 0.15, as shown in figure 9(*b*). The value of C_v is very close to those reported in Simeonov & Stern (2007, 2008).

As shown in figure 6(*a*), the layering intrusion in the present flow is of diffusive type. For such a type of intrusion, the horizontal Nusselt number of temperature Nu_T^h can be related to the isohaline slope a by the scaling law $Nu_T^h \sim a^{-1/2}$ (Simeonov & Stern 2008). Here, Nu_T^h represents the ratio of the horizontal heat flux to the horizontal temperature gradient, namely $Nu_T^h = \langle vT\rangle_h/(\kappa_T\Delta_T^h L^{-1})$. The average $\langle\rangle_h$ is conducted over the streamwise cross-section at $y = 3L/8$ and over time, and Δ_T^h is again taken as the averaged temperature difference between two endwalls in the streamwise direction. The isohaline slope is estimated by averaging over the main intrusion region, as explained in § 4.1. Figure 9(*c*) displays the dependence of Nu_T^h vs $a^{-1/2}$. The data roughly follow the scaling law $Nu_T^h \sim 128.8a^{-1/2}$, where the prefactor is fixed by linear fitting.

4.4. *The global transport*

Finally, we proceed to analyse the global transport properties in the horizontal direction. Due to our specific flow configuration, both heat and salinity are transported into the domain from the right part of the top surface with higher temperature and salinity, then move horizontally towards the left side within the domain bulk and finally exit the domain over the left part of the top surface with lower temperature and salinity. Such behaviours are shown in figure 10 by the distributions of local Nusselt number over the top boundary for case 2. The local Nusselt number is calculated as $Nu_\zeta^l = (-\kappa_\zeta\partial_z\overline{\overline{\zeta}})/(\kappa_\zeta\Delta_\zeta L^{-1})$ with $\zeta = T$ or S. The zero point of Nu^l is not at the middle point $z = L/2$ but shifted towards the warm salty end, which happens for all the four cases considered. Near the left end the vertical flux is generated by the diffusive DDC process, while near the right end it is generated by the fingering DDC. In between, the positive and negative peaks next to the zero point are caused by the upward-shifting layers when they reach the top surface.

Moreover, the total flux through the entire top surface oscillates around zero with a very long period. For example, case 1 has a time period of approximately 3000 time units, as shown in figure 2. Nevertheless, the temporally averaged total flux should be approximately zero when the system is in the statistically steady state and the average is calculated over a long enough time period. We measure these global fluxes Nu_ζ by integrating Nu_ζ^l over the range at either side of the zero-flux point. In addition, we define the horizontal Rayleigh number $Ra_L = (g\beta_T L^3\Delta_T)/(\nu\kappa_T)$ to account for the effect

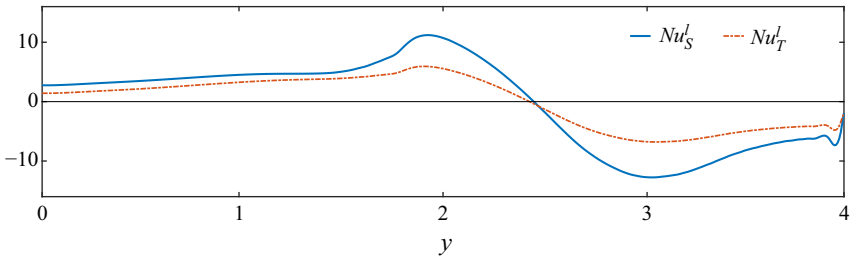

Figure 10. The local Nusselt number Nu^l over the top boundary for case 2.

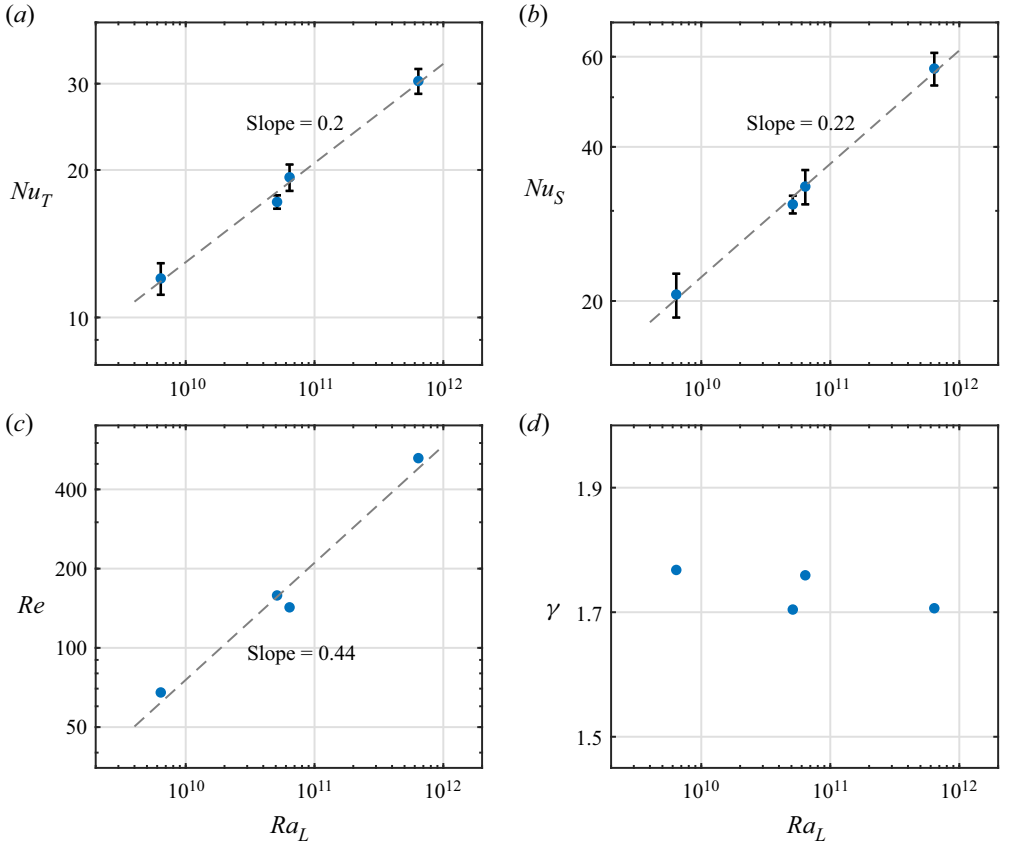

Figure 11. The global responses vs the horizontal Rayleigh number Ra_L. (*a*) The global heat flux. (*b*) The global salinity flux. (*c*) The Reynolds number. (*d*) The horizontal density flux ratio γ. In (*a*,*b*) the error bars indicate the maximal deviation from zero of the total fluxes through the top surface.

of the streamwise length L. The dependences of Nu_T and Nu_S on Ra_L are plotted in figures 11(*a*) and 11(*b*), respectively. Both Nusselt numbers follow a very similar scaling law: $Nu_\zeta \sim Ra_L^{\alpha_\zeta}$ with α_ζ very close to 0.2. The Reynolds number $Re = U_{rms}L/\nu$ follows a scaling law of $Re \sim Ra_L^{0.44}$. Here, U_{rms} is the root-mean-square value of the velocity magnitude.

Since both the heat and salinity fluxes have very similar scaling behaviours, the density flux ratio $\gamma = (\beta_T\langle vT\rangle_0)/(\beta_S\langle vS\rangle_0)$ should be nearly constant for different Ra_L.

The average $\langle\,\rangle_0$ is conducted over the streamwise cross-section at the zero-flux point of the top boundary, and over time. Figure 11(*d*) shows that γ lies between 1.7 and 1.8. Nearly constant γ implies that the ratio of the density anomaly flux due to the heat flux to that due to the salinity flux exhibits very weak dependence on Ra_L. Moreover, $\gamma > 1$ indicates that the net density anomaly flux is in the same direction as the scalar gradients along the top boundary.

5. Conclusion

In summary, we demonstrate that horizontal temperature and salinity gradients, which have compensated effects on density, can induce thermohaline intrusions in the water mass below, and interleaving layers with opposite moving directions emerge. Double diffusive mixing plays a crucial role in such a process. Different types of DDC at the warm salty end and the cold fresh end produce different vertical fluxes of heat and salinity, which maintain the horizontal scalar differences at the lower part of the domain and the generation of intrusion layers. The main intrusion region is located close to the cold and fresh side with the layers, sloping upward towards the warm and salty side, therefore the intrusion layering is of the diffusive type. At the interfaces between interleaving layers, fingering and diffusive DDC happen alternatively.

The layers do not hold their heights but shift upward with a very small velocity. This is caused by the divergence of vertical fluxes through the top surface. Specifically, the density fluxes induced by the heat and salinity fluxes at the two ends of top surfaces do not balance each other, and a density difference accumulates in the streamwise direction at the lower part. New layers emerge periodically close to the bottom boundary and shift the existing layers upward.

Detailed inspections suggest that the current intrusion and interleaving layers fit into the narrow front type according to the theoretical model of Niino (1986). Both the layer thickness and current velocity exhibit similar scaling laws as those for the intrusion in narrow fronts. The horizontal Nusselt number of temperature roughly follows a power-law scaling of the isohaline slope with an exponent $-1/2$. The total horizontal fluxes through the fluid layer can be described by the scaling laws of the horizontal Rayleigh number. The density flux ratio in the horizontal direction is nearly constant for all cases and higher than unity. Therefore, both heat and salinity are transferred from the warm salty side to the cold fresh side, but the density anomaly is transferred in the opposite direction.

Our results extend the circumstance where intrusions may occur. Specifically, they not only develop within the water mass of horizontal gradients, but also in the fluid body at adjacent depths. Based on a symmetry argument, one can expect that scalar gradients at bottom boundary should also induce similar intrusions above. Also, horizontal temperature and salinity gradients drive horizontal fluxes in the adjacent fluid layers, which may accelerate the decay of the horizontal scalar inhomogeneity. All these findings are of great interest and deserve experimental and observational verification. More studies are also needed to fully understand the intrusion flows presented here. For instance, the influences of the domain aspect ratio and the density ratio are not yet touched upon. The Schmidt number is much smaller than those in the ocean, and simulations with typical oceanic Schmidt number are highly desired in the future.

Supplementary movie. Supplementary movie is available at https://doi.org/10.1017/jfm.2021.753.

Funding. This work is supported by the Major Research Plan of the National Natural Science Foundation of China for Turbulent Structures under the grants 91852107 and 91752202. Y.Y. also acknowledges the partial

support from the Strategic Priority Research Program of Chinese Academy of Sciences under the grant no. XDB42000000.

Declaration of interests. The authors report no conflict of interest.

Author ORCIDs.
Yantao Yang https://orcid.org/0000-0001-5065-2769.

References

Bebieva, Y. & Timmermans, M.-L. 2019 Double-diffusive layering in the Canada basin: an explanation of along-layer temperature and salinity gradients. *J. Geophys. Res.* **124**, 723–735.

Chen, C.F. 1974 Onset of cellular convection in a salinity gradient due to a lateral temperature gradient. *J. Fluid Mech.* **63** (3), 563–576.

Hebert, M.A. 2011 Numerical simulations, mean field theory and modulational stability analysis of thermohaline intrusions. Thesis, Naval Postgraduate School, Monterey, CA, USA.

Holbrook, W.S., Paramo, P., Pearse, S. & Schmitt, R.W. 2003 Thermohaline fine structure in an oceanographic front from seismic reflection profiling. *Science* **301**, 821–824.

Kerr, O.S 1989 Heating a salinity gradient from a vertical sidewall: linear theory. *J. Fluid Mech.* **207**, 323–352.

Krishnamurti, R. 2006 Double-diffusive interleaving on horizontal gradients. *J. Fluid Mech.* **558**, 113–131.

Lee, J.H. & Richards, K.J. 2004 The three-dimensional structure of the interleaving layers in the western equatorial Pacific ocean. *Geophys. Res. Lett.* **31**, L07301.

Malki-Epshtein, L., Phillips, O.M. & Huppert, H.E. 2004 The growth and structure of double-diffusive cells adjacent to a cooled sidewall in a salt-stratified environment. *J. Fluid Mech.* **518**, 347–362.

Merryfield, W.J. 2000 Origin of thermohaline staircases. *J. Phys. Oceanogr.* **30**, 1046–1068.

Niino, H. 1986 A linear stability theory of double-diffusive horizontal intrusions in a temperature–salinity front. *J. Fluid Mech.* **171**, 71–100.

Ostilla-Mónico, R., Yang, Y., van der Poel, E.P., Lohse, D. & Verzicco, R. 2015 A multiple resolutions strategy for direct numerical simulation of scalar turbulence. *J. Comput. Phys.* **301**, 308–321.

Paparella, F. & von Hardenberg, J. 2012 Clustering of salt fingers in double-diffusive convection leads to staircaselike stratification. *Phys. Rev. Lett.* **109**, 014502.

Radko, T. 2013 *Double-Diffusive Convection*. Cambridge University Press.

Radko, T. & Sisti, C. 2017 Life and demise of intrathermocline mesoscale vortices. *J. Phys. Oceanogr.* **47**, 3087–3103.

Ruddick, B. 1983 A practical indicator of the stability of the water column to double-diffusive activity. *Deep-Sea Res.* A **30** (10), 1105–1107.

Ruddick, B. 2003 Laboratory studies of interleaving. *Prog. Oceanogr.* **56**, 529–547.

Ruddick, B. & Kerr, O. 2003 Oceanic thermohaline intrusions: theory. *Prog. Oceanogr.* **56**, 483–497.

Ruddick, B., Oakey, N.S. & Hebert, D. 2010 Measuring lateral heat flux across a thermohaline front: a model and observational test. *J. Mar. Res.* **68**, 523–439.

Ruddick, B. & Richards, K. 2003 Oceanic thermohaline intrusions: observations. *Prog. Oceanogr.* **56**, 499–527.

Ruddick, B.R. & Turner, J.S. 1979 The vertical length scale of double-diffusive intrusions. *Deep-Sea Res.* A **26** (8), 903–913.

Sarkar, S., Sheen, K.L., Klaeschen, D., Brearley, J.A., Minshull, T.A., Berndt, C., Hobbs, R.W. & Naveira Garabato, A.C. 2015 Seismic reflection imaging of mixing processes in Fram strait. *J. Geophys. Res.* **120**, 6884–6894.

Simeonov, J. & Stern, M.E. 2004 Double-diffusive intrusions on a finite-width thermohaline front. *J. Phys. Oceanogr.* **34**, 1723–1740.

Simeonov, J. & Stern, M.E. 2007 Equilibration of two-dimensional double-diffusive intrusions. *J. Phys. Oceanogr.* **34**, 625–643.

Simeonov, J. & Stern, M.E. 2008 Double-diffusive intrusions in a stable salinity gradient 'heated from below'. *J. Phys. Oceanogr.* **38** (10), 2271–2282.

Stellmach, S., Traxler, A., Garaud, P., Brummell, N. & Radko, T. 2011 Dynamics of fingering convection. Part 2. The formation of thermohaline staircases. *J. Fluid Mech.* **677**, 554–571.

Stern, M.E. 1960 The salt-fountain and thermohaline convection. *Tellus* **12** (2), 172–175.

Stern, M.E. 1967 Lateral mixing of water masses. *Deep-Sea Res.* **14**, 747–753.

STERN, M.E. 2003 Initiation of a doubly diffusive convection in a stable halocline. *J. Mar. Res.* **61** (2), 211–233.

TANG, Q., TONG, V.C.H., HOBBS, R.W. & MORALES MAQUEDA, M.A. 2019 Detecting changes at the leading edge of an interface between oceanic water layers. *Nat. Commun.* **10**, 4674.

TIMMERMANS, M.-L. & MARSHALL, J. 2020 Understanding Arctic ocean circulation: a review of ocean dynamics in a changing climate. *J. Geophys. Res.* **125**, e2018JC014378.

TOOLE, J.M. & GEORGI, D.T. 1981 On the dynamics and effects of double-diffusively driven intrusions. *Prog. Oceanogr.* **10** (2), 123–145.

VERONIS, G. 1965 On finite amplitude instability in thermohaline convection. *J. Mar. Res.* **23** (1), 1–17.

WOODS, J.D., ONKEN, R. & FISCHER, J. 1986 Thermohaline intrusions created isopycnically at oceanic fronts are inclined to isopycnals. *Nature* **322**, 446–449.

YOU, Y. 2002 A global ocean climatological atlas of the Turner angle: implications for double-diffusion and water-mass structure. *Deep-Sea Res.* **49** (11), 2075–2093.